# Heterogeneous activation of peroxymonosulfate by a novel magnetic 3D γ-MnO$_2$@ZnFe$_2$O$_4$/rGO nanohybrid as a robust catalyst for phenol degradation

Amr Hussein Mady[a,b], Marjorie Lara Baynosa[a], Dirk Tuma[c], Jae-Jin Shim[a,*]

[a] School of Chemical Engineering, Yeungnam University, Gyeongsan, Gyeongbuk 38541, Republic of Korea
[b] Petrochemical Department, Egyptian Petroleum Research Institute, Nasr City, Cairo 11727, Egypt
[c] BAM Federal Institute for Materials Research and Testing, Richard-Willstätter-Str. 11, 12489 Berlin, Germany

ABSTRACT

Three-dimensional (3D) γ-MnO$_2$@ZnFe$_2$O$_4$/reduced graphene oxide (rGO) nanohybrids were synthesized using a one-pot hydrothermal self-assembly method. The morphology and properties of the nanohybrids were investigated. The synergistic interactions among γ-MnO$_2$, ZnFe$_2$O$_4$, and rGO resulted in 3D nanoflakes distributed uniformly in the rGO structure with a thickness of approximately 2–5 nm, leading to a high surface area. The nanohybrid containing 10 wt. % rGO exhibited superior catalytic activities for phenol degradation through the activation of peroxymonosulfate (PMS) to generate active sulfate radicals (SO$_4^{\bullet-}$). Typically, 50 mL of a 20 ppm phenol solution was degraded completely and 85% of the carbon content had been mineralized in 30 min at 25 °C using 10 mg of the nanohybrid. The nanohybrid could be recovered easily using a magnet and reused, maintaining high stability during catalytic oxidation. The 3D γ-MnO$_2$@ZnFe$_2$O$_4$/rGO nanohybrid catalyst could be applied to the removal of hard-to-degrade waste materials owing to its high efficiency and excellent reusability.

## 1. Introduction

Wastewater effluents from many industrial processes contain highly toxic refractory products, such as phenolic compounds, which can have detrimental effects on the environment and public health [1–3]. Previous research has been carried out to achieve complete degradation of these pollutants by applying advanced oxidation processes (AOPs) because of their highly efficient mineralization and non-selectivity [4–8]. Among the various AOPs, the Fenton and Fenton-like reactions are well-known and efficient reactions to degrade organic contaminants due to the generation of hydroxyl radicals (HO$^\bullet$), which are the main reactive and oxidizing radicals in reactions [5,9–11]. On the other hand, these processes have some limitations, such as obstacles in the transportation and storage of H$_2$O$_2$, pH limitations (2 to 4), metal leaching, and sludge production, which reduce their applicability [12–14].

A promising alternative similar to H$_2$O$_2$ is peroxymonosulfate (PMS). This compound can be used to generate sulfate radicals (SO$_4^{\bullet-}$), which are considered more stable and powerful than H$_2$O$_2$ and HO$^\bullet$ owing to its high redox potential ($E$ = 3.1 eV) compared to H$_2$O$_2$ ($E$ = 2.7 eV) and HO$^\bullet$. Many applications, particularly the chemical oxidation of organic contaminants, employ PMS as an environmentally friendly and inexpensive oxidant because of its selectivity, easy handling during storage and transportation, and no need for pH adjustment [13]. Several transition metals have been used to activate PMS. Among them, cobalt ions are used most extensively [15,16]. On the other hand, the leaching of cobalt, which is considered a potential carcinogen, in such reaction systems can result in serious health problems [17,18]. A feasible solution to overcome these drawbacks includes the development of novel recoverable hybrid materials that can reduce metal leaching and sustain high activity in the heterogeneous activation of PMS.

Manganese-based materials have been applied in many areas because of their superior chemical and physical properties, high abundance in soil, and low toxicity to the environment compared to cobalt [19–23]. As catalysts, they are used widely in AOPs due to the unique redox loop of manganese (Mn$^{2+}$/Mn$^{4+}$), which gives higher potential activity through a single electron transfer [23]. Nevertheless, the separation of manganese-based materials from the reaction solution is difficult because of their tendency to form superfine particles [16,18]. The intercalation of magnetic ZnFe$_2$O$_4$-based materials can enhance the

separation of the catalyst by the application of an external magnetic field while utilizing their good dispersion and high stability in water as well as the low dipole–dipole attraction between their particles compared to other magnetic-based materials [3,24]. Moreover, $ZnFe_2O_4$ can activate PMS to generate $SO_4^{\bullet-}$ through a reaction with $Fe^{2+}$ ions [25].

On the other hand, materials with three-dimensional (3D) hierarchical structures strongly affect the catalytic behaviors of the catalysts. In particular, 3D structures have a great impact on the performance of catalysts because they possess the properties of both nanostructures and bulk materials, which show attractive chemical and physical characteristics, through efficient channels for mass transportation and high surface area [26,27].

To date, only few reports have focused on the development of magnetic $MnO_2$-based catalysts for phenol degradation [3,28]. These materials, however, have very low surface areas, resulting in a long time for complete degradation. To overcome this, the introduction of graphene as a two-dimensional (2D) material with a high surface area has captured the attention of many researchers because of its outstanding properties in terms of synergistic charge delocalization, chemical stability, good conductivity, and unique electronic transport properties. With the aid of these properties, graphene is considered a promising support for coupling with other materials to address the above-mentioned problems [29–31]. Recently, Wang et al. prepared 2D/2D $\gamma$-$MnO_2$/rGO using rGO and $KMnO_4$ for the catalytic ozonation of 4-chlorophenol in the presence of PMS [7]. Ramesh et al. examined the catalytic efficiency of $MnO_2$/rGO nanowires for the degradation of Reactive Red using a sono-Fenton-assisted process in the presence of $H_2O_2$ [32]. Qu et al. used a suspension of GO/$MnSO_4$ from the modified Hummers method to fabricate rGO/$MnO_2$ to degrade Methylene Blue dye in the presence of $H_2O_2$ [30]. To the best of the authors' knowledge, however, there are no reports on the degradation of phenol using hierarchical 3D $\gamma$-$MnO_2$ supported on a magnetic $ZnFe_2O_4$/rGO nanohybrid. In the present study, a hierarchical 3D $\gamma$-$MnO_2$@$ZnFe_2O_4$/rGO nanohybrid was prepared via one-pot hydrothermal synthesis at a low temperature of 100 °C. The prepared nanohybrid exhibited the high activation of PMS, resulting in high catalytic activity for phenol degradation and low activation energy due to the synergetic effects among its components.

## 2. Experimental

### 2.1. Materials and sample synthesis

All materials in this study were of high purity grade, purchased from Sigma-Aldrich, and used as received. Graphene oxide (GO) was generated using Tour's method [33]. Scheme 1 describes the synthesis of a 3D $\gamma$-$MnO_2$@$ZnFe_2O_4$/rGO nanohybrid through the dispersion of 0.24 g of $ZnFe_2O_4$, which was synthesized previously via a hydrothermal method [34], in a sonicated aqueous solution of 80 mL GO (1 mg $ml^{-1}$) for 1 h. Subsequently, 0.45 g of $KMnO_4$ and 1 mL of HCl (37%) were added to

the previous solution with stirring for 30 min. The resulting suspension was transferred to a 120 mL autoclave and heated to 100 °C for 12 h. After the reaction, the autoclave was cooled down naturally to room temperature. The samples were then collected by centrifugation, washed with DI water, and dried in a vacuum oven at room temperature for 30 min. For comparison, $\delta$-$MnO_2$@$ZnFe_2O_4$, $\gamma$-$MnO_2$@rGO, and $ZnFe_2O_4$@rGO were also prepared using the same process described above for the 3D $\gamma$-$MnO_2$@$ZnFe_2O_4$/rGO nanohybrid by removing one component per preparation.

### 2.2. Characterization

Powder X-ray diffraction (XRD; PANalytical, X'Pert-PRO MPD) was carried out using Cu Kα radiation. The structural information of the samples was recorded using Fourier-transform infrared (FT-IR; Bio-Rad, Excalibur Series FTS 3000) spectroscopy and Raman spectroscopy (Horiba, XploRA plus). X-ray photoelectron spectroscopy. (XPS; Kratos Analytical, AXIS Nova) was used to examine the surface components of the samples. The Brunauer-Emmett-Teller (BET) specific surface area ($S_{BET}$) and pore size distribution (PSD) of the samples were investigated using a $N_2$ adsorption–desorption apparatus (Micromeritics, Micromeritics 3Flex Surface Characterization Analyzer). Field-emission scanning electron microscopy (FE-SEM; Hitachi, S-4800) and transmission electron microscopy (TEM; Philips, CM 200) were used to determine the morphology and structure of the as-prepared materials. Thermogravimetric analysis (TGA) and differential scanning calorimetry (DSC) were performed at a heating rate of 10 K $min^{-1}$ in air (TA Instruments, SDT Q600). Hydrogen temperature-programmed desorption ($H_2$-TPD) analysis was performed using a chemisorption analyzer (Micrometrics, AutoChem II 2920) equipped with a thermal conductivity detector (TCD). Magnetization measurements were carried out at room temperature using a vibrating sample magnetometer (VSM; Dexing, Model 250). The metal content of the composite was determined by inductively coupled plasma atomic emission spectroscopy (ICP-AES; PerkinElmer, Optima 8300).

### 2.3. Catalytic activity measurement

In a typical activity test, a 10 mg of catalyst was added to 50 mL of a 20 ppm phenol solution, which was then stirred for 30 min to achieve adsorption–desorption equilibrium. To start the reaction tests, 0.3 mM PMS was added to the reaction solution. At certain intervals, 1.5 mL of the aqueous sample was withdrawn using a syringe and filtered into a vial. The concentration of phenol was analyzed by high-performance liquid chromatography (HPLC; Young Lin, Series YL9100) equipped with a YL9120 UV/Vis detector; the UV wavelength was adjusted to 275 nm for phenol, hydroquinone, and catechol, and to 244 nm for p-benzoquinone. A C-18 column (Sun Fire) was used to separate the organic compounds with a mobile solution at a flow rate of 1 mL $min^{-1}$. The eluent was a mixture of water, 1 vol. % acetic acid solution, and
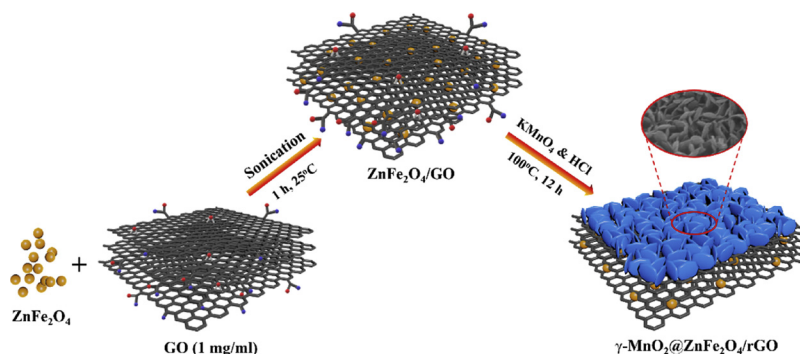


**Scheme 1.** Schematic diagram of the preparation of the 3D $\gamma$-$MnO_2$@$ZnFe_2O_4$/rGO nanohybrid by a hydrothermal method.

methanol in the ratio of 50:40:10. The total organic carbon (TOC) was measured using a TOC analyzer (Jena Analytik, multi N/C 2100S) to evaluate the mineralization of the organics during the catalytic activity process. To examine the catalytic stability and reusability, the nanohybrid was used 5 times. After each experiment, it was collected using a magnet, washed with deionized water, and dried in a vacuum oven at room temperature [29].

The reaction kinetics of phenol degradation on the nanohybrid followed the first-order kinetic model (Eq. (1)):

$$\ln\left(\frac{C}{C_0}\right) = -k_{obs}t \tag{1}$$

where $C$ is the residual concentration of phenol at time $t$; $C_0$ is the initial phenol concentration, and $k_{obs}$ is the first-order reaction rate constant. For further examinations of the reaction mechanism, two sets of quenching tests were performed to determine the reactive radical species involved in the degradation of phenol using ethanol and tert-butyl alcohol (TBA) as radical scavengers in typical activity measurements [18].

For $H_2$-TPD analysis, a 30 mg of sample was initially reduced *in situ* in a flow of 10% $H_2$/Ar at 300 °C for 2 h. The sample was then cooled to 50 °C and saturated with 10% $H_2$/Ar for 2 h, followed by purging with He for 100 min to remove any physisorbed molecules. The $H_2$-TPD experiment was performed by heating to 800 °C at a rate of 10 °C/min under a continuous flow of He gas. The turnover frequencies (*TOF*) of the synthesized catalysts were calculated as follows:

$$TOF\,(s^{-1}) = \frac{r\,v_{H_2}m_{cat}}{V_{H2\,ad}\,n} \tag{2}$$

where $r$ is the reaction rate ($s^{-1}$); $v_{H_2}$ is the molar volume of $H_2$ at STP (22,414 $cm^3$ $mol^{-1}$); $m_{cat}$ is the mass of the catalyst; $V_{H2\,ad}$ is the amount of $H_2$ adsorbed ($cm^3$ $g^{-1}$); and $n$ is the stoichiometric factor of the reaction between $H_2$ and the selected metal. The total number of moles of accessible active sites for Mn were calculated based on the results of the $H_2$ chemisorption test ($H_2$-TPD). The total metal loading in the catalysts was determined by ICP-AES. The percentage dispersion (% $D_{Mn}$) of manganese deposited on the surface is defined as follows:

$$\%\,D_{Mn} = \frac{N_s}{N_t} \tag{3}$$

where $N_s$ is the total number of exposed surface atoms of Mn and $N_t$ is the total number of metal atoms of Mn present in the sample.

## 3. Results and discussion

### 3.1. Material characterization

XRD was performed on the bare $ZnFe_2O_4$ and composites to determine the crystalline structure of the $\gamma$-$MnO_2$@$ZnFe_2O_4$/rGO nanohybrid (Fig. 1). For $ZnFe_2O_4$, the XRD peaks at 30.1, 35.26, 42.8, 53.2, 56.6, and 62.2° $2\theta$ were indexed to the (220), (311), (400), (422), (511), and (440) crystal planes of spinel $ZnFe_2O_4$ (JCPDS 22-1012), respectively, which confirmed the formation of a cubic structure. A weak broad peak was observed at 22° $2\theta$, which was indexed to the (002) plane of reduced graphene oxide in the $ZnFe_2O_4$@rGO nanocomposite. The characteristic XRD peaks of $\gamma$-$MnO_2$ were observed in both $\gamma$-$MnO_2$@rGO and the nanohybrid composite, $\gamma$-$MnO_2$@$ZnFe_2O_4$/rGO, at 22.2, 36.1, 42.2, 55.6, and 67.9° $2\theta$, which were indexed to the (101), (201), (211), (212), and (610) planes, respectively, of ramsdellite $\gamma$-$MnO_2$ (JCPDS 44-0142) [7,35,36]. Furthermore, no XRD peaks of $\delta$-$MnO_2$ were observed in the $\gamma$-$MnO_2$@$ZnFe_2O_4$/rGO nanohybrid, confirming that the $MnO_2$ is present only in the gamma ($\gamma$) form. The XRD peak for rGO was not detected in the $\gamma$-$MnO_2$@$ZnFe_2O_4$/rGO nanohybrid due to the anchoring of $ZnFe_2O_4$ NPs as spacers and 3D $\gamma$-$MnO_2$ nanoflakes on the rGO surface, which minimized the restacking of the rGO sheets.
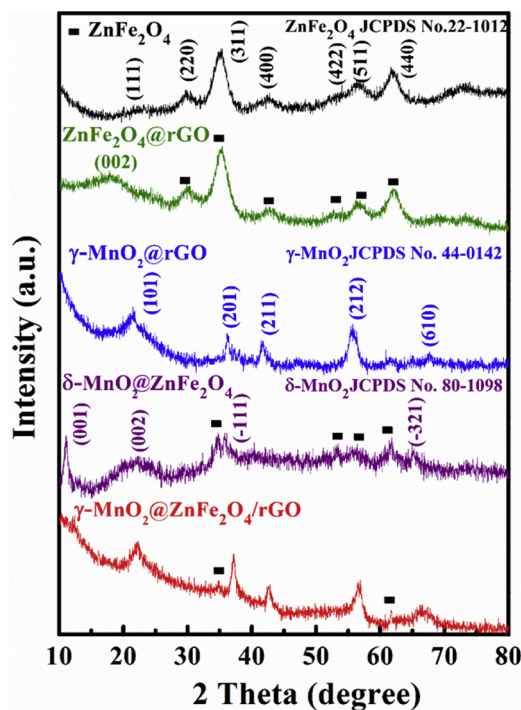


**Fig. 1.** XRD patterns of bare $ZnFe_2O_4$, $ZnFe_2O_4$@rGO, $\gamma$-$MnO_2$@rGO, $\delta$-$MnO_2$@$ZnFe_2O_4$, and $\gamma$-$MnO_2$@$ZnFe_2O_4$/rGO.

Fig. 2 presents SEM and TEM images of the samples. The as-prepared $ZnFe_2O_4$ nanoparticles exhibited a spherical morphology with a mean size of 10–20 nm (Fig. S1). Fig. 2a and b present SEM and TEM images of $ZnFe_2O_4$@rGO, respectively, which show that all $ZnFe_2O_4$ NPs were intercalated between the graphene nanosheets. The SEM (Fig. 2c) and TEM (Fig. 2d) images of $\gamma$-$MnO_2$@rGO revealed aggregated nanoflakes of $\gamma$-$MnO_2$ deposited on the rGO nanosheets. The SEM (Fig. 2e) and TEM (Fig. 2f) images of $\delta$-$MnO_2$@$ZnFe_2O_4$, which was synthesized according to the work by Wang et al. [7], showed a microspherical structure with a uniform hydrangea-like structure with a diameter of 3–5 μm. Fig. 2g and h presents SEM and TEM images of the $\gamma$-$MnO_2$@$ZnFe_2O_4$/rGO nanohybrid, respectively, which show the intimate combination of 3D $\gamma$-$MnO_2$ nanoflakes, 2–5 nm in thickness, anchored to the rGO nanosheets intercalated with $ZnFe_2O_4$. Such a combination showed high chemical performance due to the rapid transportation of electrons between the $\gamma$-$MnO_2$ nanoflakes and rGO nanosheets intercalated with $ZnFe_2O_4$ NPs [7,37].

The HRTEM image in Fig. 3a shows well-resolved lattice fringes with typical d-spacings of 0.38 and 0.25 nm, which correspond to the (201) plane of $MnO_2$ and (311) plane of $ZnFe_2O_4$, respectively. The EDS of $\gamma$-$MnO_2$@$ZnFe_2O_4$/rGO nanohybrid (Fig. 3b) indicated the presence of Mn, O, C, Fe, and trace amounts of Zn, which was due to the partial leaching of Zn from zinc ferrite after the addition of HCl during the preparation process [37]. The elemental mapping images showed that Mn, Fe, and Zn were dispersed uniformly on the rGO nanosheets, which further confirmed the successful synthesis of the $\gamma$-$MnO_2$@$ZnFe_2O_4$/rGO nanohybrid.

Based on the experimental results, a possible mechanism is proposed to understand the growth mechanism of $MnO_2$ nanoflakes on rGO sheets (Figs. S2 and S3). In the first step, $ZnFe_2O_4$ is dispersed in the graphene oxide solution by bath sonication for 1 h to intercalate the $ZnFe_2O_4$ nanoparticles between the GO sheets ($ZnFe_2O_4$@GO).

Subsequently, different amounts of $KMnO_4$ and HCl are used to induce the growth of $MnO_2$ nanoflakes. Using a small amount of $KMnO_4$ (0.15 g), the $Mn^{2+}$ ions in the solution bind with the negatively charged oxygen-containing functional groups of GO sheets via electrostatic forces [3,38]. The addition of 0.33 ml HCl to a solution of $ZnFe_2O_4$/GO
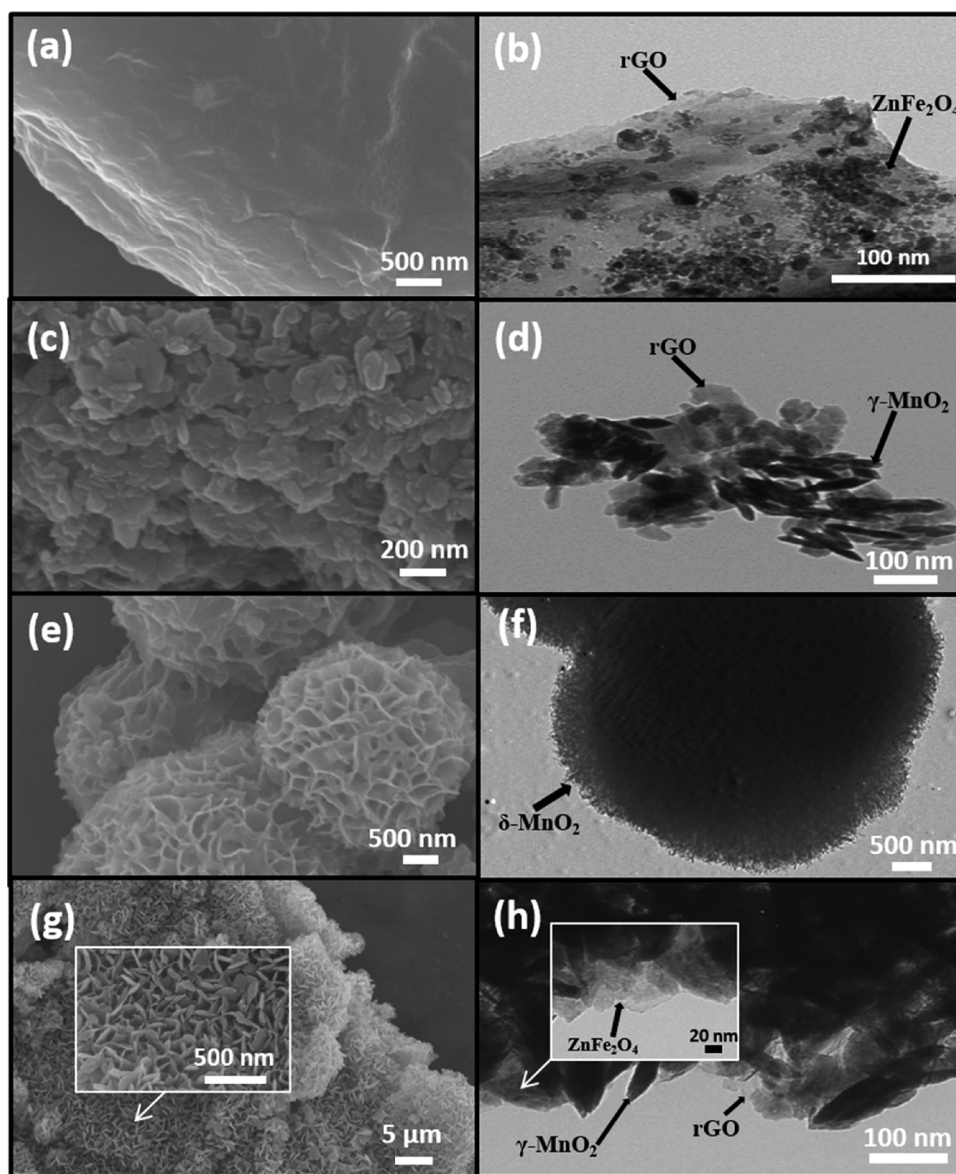
**Fig. 2.** SEM and TEM images of $ZnFe_2O_4$@rGO (a, b), $\gamma$-$MnO_2$@rGO (c, d), $\delta$-$MnO_2$@$ZnFe_2O_4$ (e, f), and $\gamma$-$MnO_2$@$ZnFe_2O_4$/rGO (g, h).

and $KMnO_4$ results in the oxidation of $Mn^{2+}$ ions to and the nucleated $MnO_2$ combines on the surface of the GO sheets and starts growing into nanoflakes (Figs. S2a and S3a). Increasing the amounts of $KMnO_4$ and HCl to 0.45 g and 1 ml, respectively, results in the formation of $MnO_2$ nanoflakes on the rGO sheets without aggregation (Figs. S2c and S3c) [39,40]. Further increases in the amounts of $KMnO_4$ and HCl to 0.6 g and 1.33 ml, respectively, produce aggregated $MnO_2$ nanoflakes on the surface of rGO (Figs. S2d and S3d).

*TOF* was determined to further compare the samples with different manganese loadings, as shown in Figure S4 and Table 1, wherein the number of phenol molecules that had been degraded per manganese atom and time unit was considered the catalytic parameter. According to the results of chemisorption analysis ($H_2$-TPD), the *TOF* values increased with increasing amounts of $KMnO_4$ up to the optimal load of 0.45 g but decreased beyond this value due to the pore-blocking effect, resulting in a decrease in total surface area (Table 1). The high efficiency may also be due to the uniform distribution of manganese on the surface of the RGO sheets, which gives a high percentage dispersion (67.8%) compared to other composites, as confirmed by SEM and TEM (Figs. S2c and S3c), and provides more active sites for PMS activation [41].

The chemical bonding state of the $\gamma$-$MnO_2$@$ZnFe_2O_4$/rGO nanohybrid was examined by XPS (Fig. 4). The survey spectrum revealed the existence of Mn 2p, Fe 2p, Zn 2p, O 1 s, and C 1 s energy regions, as shown in Fig. 4a. The Mn 2p spectrum in Fig. 4b revealed two main peaks at approximately 642.5 and 654.2 eV, corresponding to the binding energies of Mn $2p_{3/2}$ and Mn $2p_{1/2}$, respectively [30]. The spin energy separation between Mn $2p_{3/2}$ and Mn $2p_{1/2}$ was 11.7 eV, showing good agreement with the published spectra of $MnO_2$ and also revealing the formation of $MnO_2$ on the rGO/$ZnFe_2O_4$ hybrid [7]. The Fe 2p spectrum in Fig. 4c shows the binding energies of Fe $2p_{3/2}$ at 711.4 and 713.1 eV, which correspond to the octahedral and tetrahedral sites, respectively. The peak at 725.6 eV for the Fe $2p_{1/2}$ and the two shake-up satellite peaks at 719.3 and 732.5 eV suggest that only $Fe^{3+}$ exists in the $ZnFe_2O_4$ particles in the nanohybrid [29]. The Zn 2p spectrum in Fig. 4d shows two major fitting peaks centered at 1044.8 and 1021.7 eV, which were assigned to Zn $2p_{1/2}$ and Zn $2p_{3/2}$, respectively. The low intensity of these two Zn 2p peaks was attributed to the leaching of zinc from the zinc ferrite sample during preparation of the hybrid, which was also confirmed by EDS. The O 1 s region in Fig. 4f shows three fitted peaks centered at 530.0, 531.5, and 533.2 eV, which were assigned to the Mn−O−Mn, Mn−O−H, and C−O/C=O bonds,
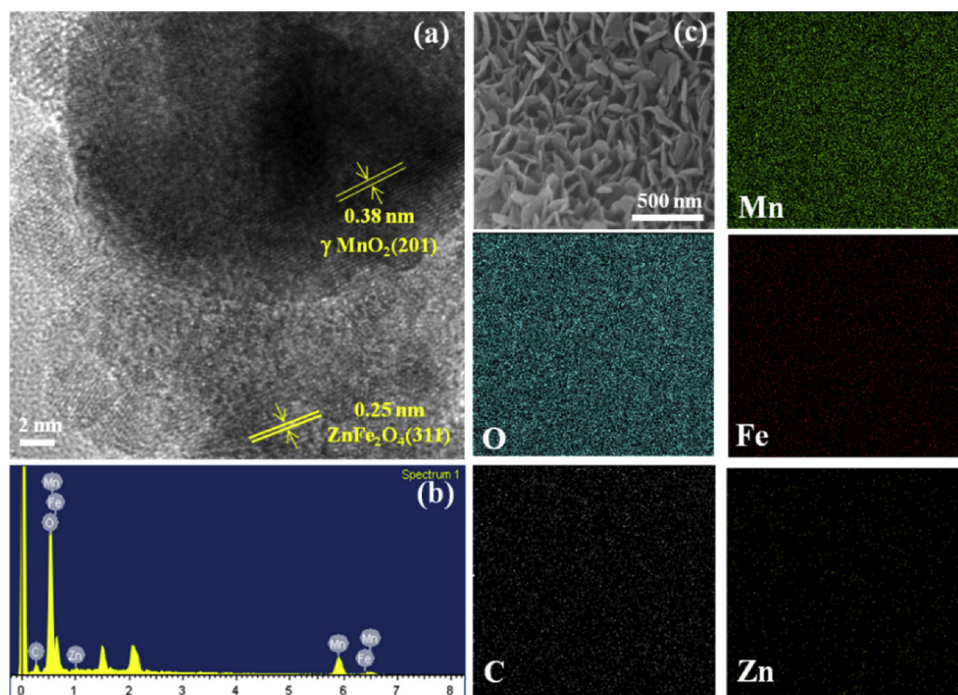
**Fig. 3.** (a) HRTEM image, (b) EDS spectrum, and (c) elemental mapping images of γ-MnO$_2$@ZnFe$_2$O$_4$/rGO.

respectively [7,30,42]. For the C 1 s spectrum in Fig. 4e, the main peak was located at 284.7 eV, which was attributed to C—C and C=C bonds, whereas the two weak peaks centered at 285.6 and 289.0 eV correspond to C—O and C=O bonds, respectively [29]. The degree of reduction of GO was calculated from the XPS data by comparing the C 1 s spectra of the nanohybrid (Fig. 4e) and GO (Fig. S5). The amount of oxygenated carbon (including C—O, C=O, and O—C=O) decreased from 88% in GO to 45.48% in the nanohybrid, confirming the reduction of GO during the hydrothermal treatment.

Fig. 5a shows the Raman spectra of both GO and γ-MnO$_2$@ZnFe$_2$O$_4$/rGO nanohybrid. Two characteristic peaks corresponding to the D-band (1360 cm$^{-1}$), which originates from the disorder and defects of carbon materials, and the G-band (1589 cm$^{-1}$), which was attributed to the vibration of the sp$^2$-hybridized carbon, were present in both samples. After the hydrothermal reduction treatment, the $I_D/I_G$ intensity ratio for GO (0.906) increased to 1.308 in the γ-MnO$_2$@ZnFe$_2$O$_4$/rGO nanohybrid due to an increase in the degree of defects and disorder and a decrease in the mean size of the sp$^2$ domains [29]. The increase in the $I_D/I_G$ ratio confirms that GO had been deoxygenated and reduced to rGO. The peak at 646 cm$^{-1}$ corresponds to the A$_g$ mode of MnO$_2$, which originates from the MnO$_6$ octahedral breathing vibrations. This shows that MnO$_2$ had been anchored successfully on the rGO sheets [42].

Evidence for the reduction of oxygen functional groups on the GO surface was obtained from the FT-IR spectra of GO and γ-MnO$_2$@

ZnFe$_2$O$_4$/rGO nanohybrid, as shown in Fig. 5b. The characteristic peaks of GO can be observed at 1056.81 cm$^{-1}$ (stretching vibrations of epoxy groups, C—O), 1398.49 cm$^{-1}$ (O—H deformation vibrations of tertiary C—OH), 1625.31 cm$^{-1}$ (O—H deformation vibrations of COOH groups), and 1721.04 cm$^{-1}$ (C=O stretching vibrations of COOH groups). The broad absorption peak from 3100 to 3700 cm$^{-1}$ was assigned to the O—H stretching vibration. In contrast, after the hydrothermal reduction treatment, most of the oxygen-containing functional groups had been minimized. The C=O band disappeared, and the band intensities of O—H and C—O decreased, indicating the partial reduction of GO. Finally, the two strong absorption peaks in the spectrum of γ-MnO$_2$@ZnFe$_2$O$_4$/rGO at lower wavelengths of 722.1 and 550 cm$^{-1}$ were assigned to the stretching vibrations of Mn—O—C and Fe—O bonds, respectively, and the weak adsorption peak at 433.9 cm$^{-1}$ was attributed to the Zn—O bond due to the leaching of zinc, as mentioned above.

The $S_{BET}$ and PSD of the γ-MnO$_2$@ZnFe$_2$O$_4$/rGO were investigated, as shown in Fig. 5c. According to the IUPAC classification, the γ-MnO$_2$@ZnFe$_2$O$_4$/rGO nanohybrid showed a type IV isotherm with an H3 hysteresis loop, indicating its mesoporous nature. The $S_{BET}$ of γ-MnO$_2$@ZnFe$_2$O$_4$/rGO was calculated to be 376.88 m$^2$ g$^{-1}$. The inset in Fig. 5c presents the PSD of γ-MnO$_2$@ZnFe$_2$O$_4$/rGO, showing a sharp maximum at approximately 3.5 nm and a broad peak at 5.5 nm with a corresponding average pore diameter of 8.15 nm, which guarantees the efficient transportation of pollutants to the active sites of the catalysts

**Table 1**
Turnover frequencies (TOF) for phenol degradation and the percentage dispersion of Mn over the nanohybrid surface for the γ-MnO$_2$@ZnFe$_2$O$_4$/rGO nanohybrids synthesized at different KMnO$_4$ loadings.

| γ-MnO$_2$@ ZnFe$_2$O$_4$/rGO with different KMnO$_4$ loadings (g) | Reaction rate (mol s$^{-1}$) | Moles of Mn on the surface of the sample (× 10$^3$)[a] (mol g$^{-1}$) | TOF[a] × 10$^8$ (s$^{-1}$) | Total moles of metal on sample (× 10$^3$)[b] (mol g$^{-1}$) | Mn dispersion on the catalyst (%) |
|---|---|---|---|---|---|
| 0.1125 | $5.12 \times 10^{-10}$ | 0.82 | 2.1 | 8.4 | 9.8 |
| 0.225 | $2.68 \times 10^{-9}$ | 3.5 | 2.6 | 14.5 | 24.1 |
| 0.45 | $1.67 \times 10^{-8}$ | 11.6 | 4.7 | 17.1 | 67.8 |
| 0.6 | $1.5 \times 10^{-8}$ | 13.9 | 3.6 | 22.4 | 62.1 |

[a] Estimated according to TPD analysis.
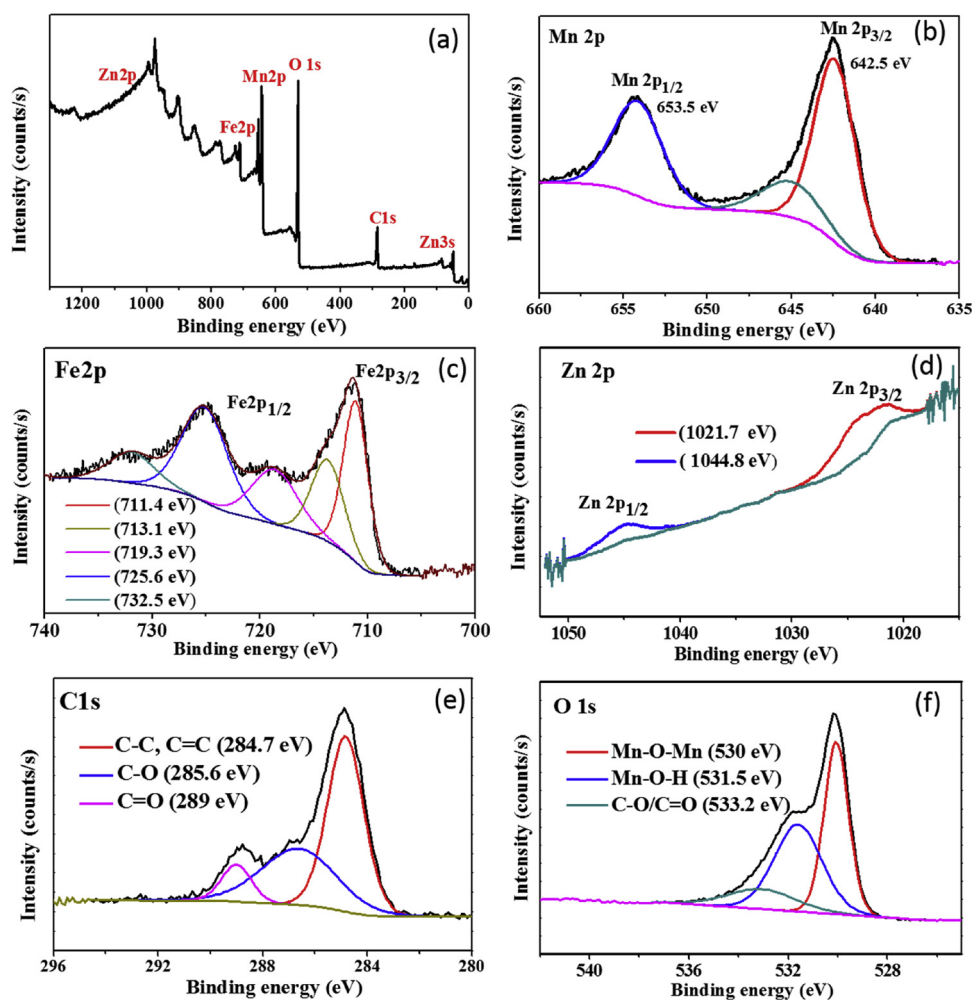[b] Estimated according to ICP analysis.

**Fig. 4.** XPS spectra of the γ-MnO₂@ZnFe₂O₄/rGO nanohybrid: (a) survey scan, (b) Mn 2p, (c) Fe 2p, (d) Zn 2p, (e) C 1 s, and (f) O 1 s energy regions.
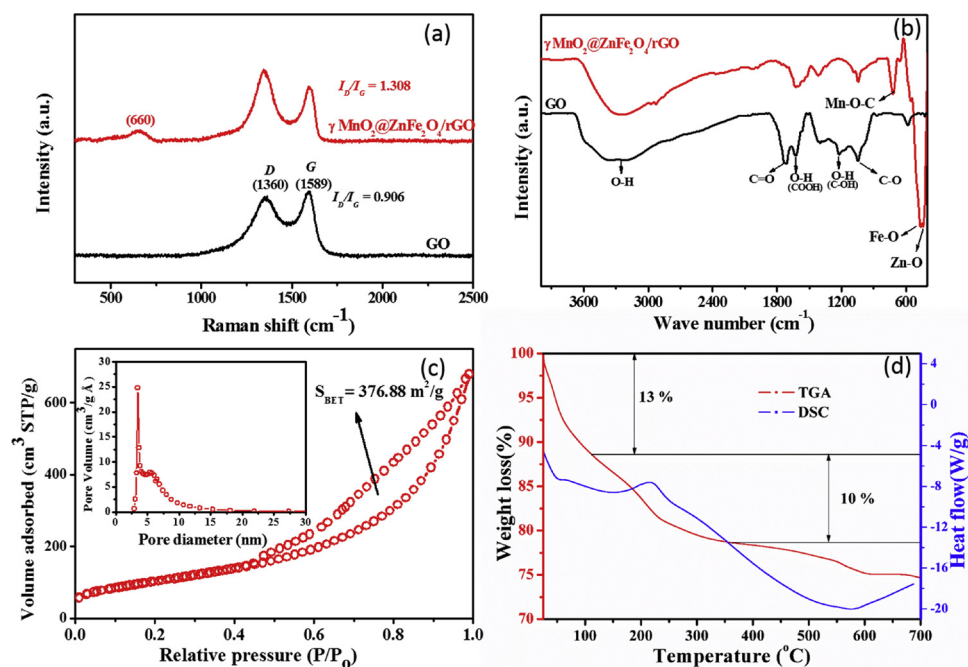


**Fig. 5.** (a) Raman spectra of GO and γ-MnO₂@ ZnFe₂O₄/rGO nanohybrid, (b) FT-IR spectra of GO and γ-MnO₂@ZnFe₂O₄/rGO nanohybrid, (c) N₂ adsorption–desorption isotherm of γ-MnO₂@ZnFe₂O₄/rGO nanohybrid (the inset presents the corresponding pore size distribution (PSD)), and (d) TGA and DSC curves of γ-MnO₂@ZnFe₂O₄/rGO nanohybrid measured in air atmosphere.

**Table 2**
Textural properties of γ-MnO$_2$@ ZnFe$_2$O$_4$/rGO and other composites and their activity in the degradation of phenol.

| Sample | $S_{BET}$ (m$^2$ g$^{-1}$) | Pore Volume (cm$^3$ g$^{-1}$) | Average pore diameter (nm) | First order rate constant (min$^{-1}$) | $R^2$ |
|---|---|---|---|---|---|
| γ-MnO$_2$@ZnFe$_2$O$_4$/rGO | 376.9 | 1.055 | 8.15 | 0.094 | 0.9912 |
| δ-MnO$_2$@ZnFe$_2$O$_4$ | 223.0 | 0.942 | 16.66 | 0.033 | 0.972 |
| γ-MnO$_2$@rGO | 46.0 | 0.246 | 24.98 | 0.0235 | 0.988 |
| ZnFe$_2$O$_4$@rGO | 153.9 | 0.339 | 8.13 | 0.0114 | 0.983 |

(Table 2). The high surface area provides more adsorption/reaction sites for PMS activation during the catalytic reaction, which result in higher catalytic activity.

TGA was performed in air to determine the thermal stability of γ-MnO$_2$@ZnFe$_2$O$_4$/rGO (Fig. 5d). Three distinct weight losses representing the loss of free and bound moisture (13 wt. %) in the range of 25 to 100 °C, the loss of oxygenated functional groups and the burn-out of graphene (10 wt. %) in the second stage between 125 and 525 °C, and the phase change of MnO$_2$ were observed in the TGA curve [43]. From the DSC profile, the strong exothermic peak at 200 °C was assigned to the combustion and decomposition of the carbon skeleton, whereas the second peak at 550 °C resulted from the conversion of MnO$_2$ to Mn$_2$O$_3$ through oxygen loss from the MnO$_2$ lattice [29–31].

### 3.2. Catalytic activity

The catalytic performance of the γ-MnO$_2$@ZnFe$_2$O$_4$/rGO nanohybrid and the other composites for phenol degradation via PMS activation was investigated (Fig. 6a). Control experiments using PMS only and γ-MnO$_2$@ZnFe$_2$O$_4$/rGO nanohybrid without PMS were also conducted. The γ-MnO$_2$@ZnFe$_2$O$_4$/rGO nanohybrid showed the highest efficiency among all the samples tested. In the absence of a catalyst, PMS cannot be activated and the amount of sulfate radicals SO$_4^{\bullet-}$ generated was insufficient to degrade the 20 ppm phenol solution [44]. The use of the γ-MnO$_2$@ZnFe$_2$O$_4$/rGO nanohybrid without the addition of PMS resulted in the adsorption of approximately 20% phenol after 3 h. By combining PMS with the composites, PMS was activated on the active sites of the metal oxides, and the catalytic activity of the composites was observed in the following order: γ-MnO$_2$@ZnFe$_2$O$_4$/rGO > δ-MnO$_2$@ZnFe$_2$O$_4$ > γ-MnO$_2$@rGO > ZnFe$_2$O$_4$@rGO.

The γ-MnO$_2$@ZnFe$_2$O$_4$/rGO nanohybrid showed complete degradation of 20 mg L$^{-1}$ (20 ppm) phenol after 30 min in the presence of PMS. A comparison with the results of the other composites revealed 22, 39, and 41% phenol degradation on ZnFe$_2$O$_4$@rGO, γ-MnO$_2$@rGO, and δ-MnO$_2$@ZnFe$_2$O$_4$, respectively, indicating the synergetic catalytic effects of combining MnO$_2$, ZnFe$_2$O$_4$, and rGO into a nanohybrid. This high efficiency may be attributed to the high surface area of the nanohybrid compared to the other composites (Table 2) and the ability of both MnO$_2$ and ZnFe$_2$O$_4$ to activate PMS through an electron transfer mechanism to produce sulfate radicals (SO$_4^{\bullet-}$) (Eqs. (5)–(7)). As a result, the composites containing both MnO$_2$ and ZnFe$_2$O$_4$ showed high efficiency compared to other composites lacking one of them (Fig. 6a). In addition, the rGO sheets increased the adsorption property of the nanohybrids through π–π stacking interactions between phenol and the aromatic regions of the graphene sheets [45]. Moreover, the uniform dispersion of MnO$_2$ nanoflakes over the rGO surface (EDS, Fig. 3c) provides more active sites for phenol degradation. The high efficiency of the nanohybrid may also be due to the strong interactions between MnO$_2$ and graphene (Mn–O–C), which was confirmed by the O 1 s deconvolution of the XPS data (Fig. 4f). Further evidence of the synergetic effects of the three components includes the total organic carbon (TOC) measurements, which revealed a significant decline (∼95%) in the organic content of the phenol solution after 180 min (Fig. S6).

A further examination of the performance of the γ-MnO$_2$@ZnFe$_2$O$_4$/rGO nanohybrid under different reaction conditions was carried out. The effects of the catalyst loading and PMS loading were studied (Fig. 6c and d). The efficiency of phenol degradation increased with increasing amounts of nanohybrid and PMS due to an increase in the number of active sites and active sulfate radicals (SO$_4^{\bullet-}$), respectively. Fig. 6b shows the effects of varying the initial phenol concentrations
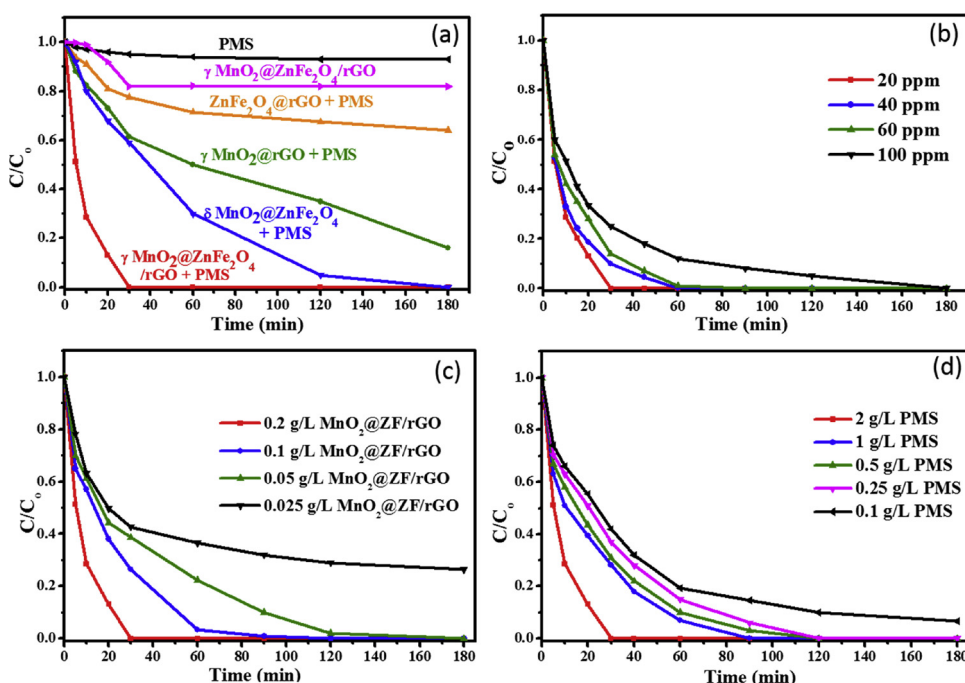
**Fig. 6.** (a) Degradation of phenol (20 mg L$^{-1}$) using different materials, (b) effect of the phenol concentration on the catalytic activity of γ-MnO$_2$@ZnFe$_2$O$_4$/rGO nanohybrid under the reaction conditions: catalyst loading = 0.2 g L$^{-1}$, PMS loading = 2.0 g L$^{-1}$ (3 mM), temperature = 25 °C, (c) effect of catalyst loading in the presence of 20 ppm phenol and 2 g L$^{-1}$ PMS, and (d) effect of PMS loading in the reaction in the presence of 20 ppm phenol and 0.2 g L$^{-1}$ catalyst.
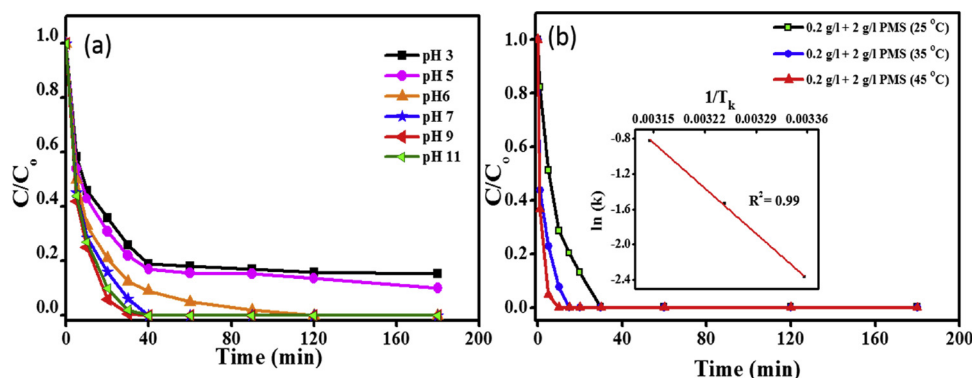
**Fig. 7.** Effects of (a) pH and (b) temperature on the catalytic activity of $\gamma$-MnO$_2$@ZnFe$_2$O$_4$/rGO nanohybrid at the reaction conditions: catalyst loading = 0.2 g L$^{-1}$, PMS loading = 2.0 g L$^{-1}$ (3 mM), initial temperature = 25 °C. The inset in (b) presents the estimation of activation energy.

from 20 to 100 mg L$^{-1}$ on the degradation efficiency of phenol. The phenol degradation efficiency decreased with increasing initial phenol concentration. At an initial concentration of 20 mg L$^{-1}$, complete removal of phenol was achieved in 30 min, whereas complete degradation was obtained in 60, 90, and 180 min at 40, 60, and 100 mg L$^{-1}$ phenol concentrations, respectively. At higher phenol concentrations, complete degradation was still achieved using 0.2 g L$^{-1}$ nanohybrid and 2.0 g L$^{-1}$ PMS, but longer reaction times were needed because at higher phenol concentrations, the reactive sites on the nanohybrid surface will be covered, leading to a decrease in PMS activation and an insufficient amount of sulfate radicals (SO$_4^{\bullet-}$) generated in the solution to readily degrade 100% of the phenol present in the solution [18,46].

The influence of pH from 3 to 11 was examined using the $\gamma$-MnO$_2$@ZnFe$_2$O$_4$/rGO nanohybrid/PMS system for phenol degradation (Fig. 7a). The degradation efficiency was enhanced markedly as the pH was increased from 3 to 9. This can be explained as follows. In the solutions with pH from 3 to 7, the surface of the catalyst (MnO$_2$ flakes) was covered with protons and only a small amount of the HSO$_5^-$ anions could adsorb on the catalyst through weak electrostatic interactions with the protons. This retarded the adsorption of HSO$_5^-$ anions and the formation of SO$_4^{\bullet-}$, as well as the loss of catalyst by leaching under acidic conditions (low pH in Table S1). In this low pH region, SO$_4^{\bullet-}$ is the only predominant radical [15,47]. The solutions with pH from 7 to 9 show similar phenol degradation efficiency due to the presence of both SO$_4^{\bullet-}$ and HO$^{\bullet}$, which are formed from a reaction of SO$_4^{\bullet-}$ with HO$^-$ to form HO$^{\bullet}$ at higher pH [48]. The electron spin resonance (ESR) results reported by Norman and Dogliotti are in agreement with these results, where the conversion of SO$_4^{\bullet-}$ to HO$^{\bullet}$ plays a more significant role [47,49,50]. The solution at pH 11 showed lower degradation efficiency than the solution at pH 9 due to the self-decomposition of HSO$_5^-$ through the scavenging of the generated SO$_4^{\bullet-}$ by another SO$_4^{\bullet-}$ (Eq. (4)) [25].

$$SO_4^{\bullet-} + SO_4^{\bullet-} \rightarrow S_2O_8^{2-} \tag{4}$$

AOPs depend on many factors; the most influential operating factor is the reaction temperature. The catalytic performance of the $\gamma$-MnO$_2$@ZnFe$_2$O$_4$/rGO nanohybrid on phenol degradation was examined at various temperatures in the presence of PMS, as shown in Fig. 7b. The first-order reaction plots of phenol degradation at various temperatures

**Table 3**
Kinetic rate constant of $\gamma$-MnO$_2$@ ZnFe$_2$O$_4$/rGO in the activation of PMS for the degradation of phenol at different temperatures.

| Catalyst | $T$ (°C) | $k_{obs}$ (min$^{-1}$) | $R^2$ | $E_a$ (kJ mol$^{-1}$) | $R^2$ |
|---|---|---|---|---|---|
| $\gamma$-MnO$_2$@ZnFe$_2$O$_4$/rGO | 25 | 0.094 | 0.9912 | | |
| | 35 | 0.238 | 0.9947 | 41.5 | 0.99 |
| | 45 | 0.438 | 0.9933 | | |

showed high regression coefficients ($R^2$), as shown in Fig. S7 and Table 3. At elevated temperatures, the phenol degradation rate increased dramatically. As the reaction temperature was changed from 25 °C to 45 °C, the $k_{obs}$ values of phenol degradation increased significantly from 0.094 min$^{-1}$ to 0.438 min$^{-1}$ (Table 3). This trend suggests that the phenol degradation process is endothermic, in which an increase in temperature improves the activation of PMS and accelerates the generation of SO$_4^{\bullet-}$ [46]. The activation energy ($E_a$) of the reaction, which was calculated by plotting ln ($k_{obs}$) vs. $1/T_k$ based on the Arrhenius equation, was 41.5 kJ mol$^{-1}$ (inset in Fig. 7b). This value is smaller than those of other reported magnetic MnO$_2$ materials [3].

The catalytic stability and recyclability of the $\gamma$-MnO$_2$@ZnFe$_2$O$_4$/rGO nanohybrid were evaluated from successive catalytic experiments by taking advantage of the magnetic property of the nanohybrid, which exhibited paramagnetic behavior and a slim hysteresis loop (Fig. 8a and inset) with a saturation magnetization value of approximately 7 emu g$^{-1}$ at 20,000 Oe, magnetic coercivity ($H_C$) of 293.67 Oe, and remanence ($M_R$) of 0.266 emu g$^{-1}$. The $\gamma$-MnO$_2$@ZnFe$_2$O$_4$/rGO nanohybrid showed a similar rate of phenol degradation after five cycles, as shown in Fig. 8b, indicating the potential of the nanohybrid for use in successive operations. The used nanohybrid was stable even after five cycles, as observed from the TEM and SEM images (Figs. S8 and S9), XRD pattern (Fig. S10), and FT-IR spectrum (Fig. S11). The XPS spectra of the Mn 2p region of the fresh and used nanohybrids further confirmed the stable structure of the material, as shown in Fig. S12, where the composition of Mn(IV) showed no significant change after the catalytic reaction. These results prove the excellent long-term stability and reusability of the $\gamma$-MnO$_2$@ZnFe$_2$O$_4$/rGO nanohybrid for phenol degradation compared to other published materials (Fig. 9 and Table S2) [6,20,23,28,51].

The catalytic degradation of phenol on the nanohybrid with the addition of PMS involves the generation of SO$_4^{\bullet-}$ and/or HO$^{\bullet}$ as reactive species. To determine the main oxidant responsible for the degradation of phenol, individual scavengers were added to the reaction medium. TBA was added as scavenger for HO$^{\bullet}$ but not for SO$_4^{\bullet-}$ and ethanol for both SO$_4^{\bullet-}$ and HO$^{\bullet}$. Figure S13a presents the results after adding the scavengers to the quenching tests. The addition of TBA only affected the rate of the catalytic reaction slightly, whereas the addition of ethanol resulted in a remarkable decrease in catalytic efficiency (from 100% to 18% after 30 min), implying a minor role of HO$^{\bullet}$ on phenol degradation. Therefore, SO$_4^{\bullet-}$ is considered the dominant contributor in the catalytic degradation of phenol. The intermediate products during the phenol degradation reaction were detected by HPLC, as shown in Fig. S13b. The results revealed p-benzoquinone (BZQ) and hydroquinone to be the major intermediates in the reaction, which showed that hydroxylation occurs at the para position rather than at the ortho position (1,2-dyhydroxybenzene) (Fig. S14) [27].

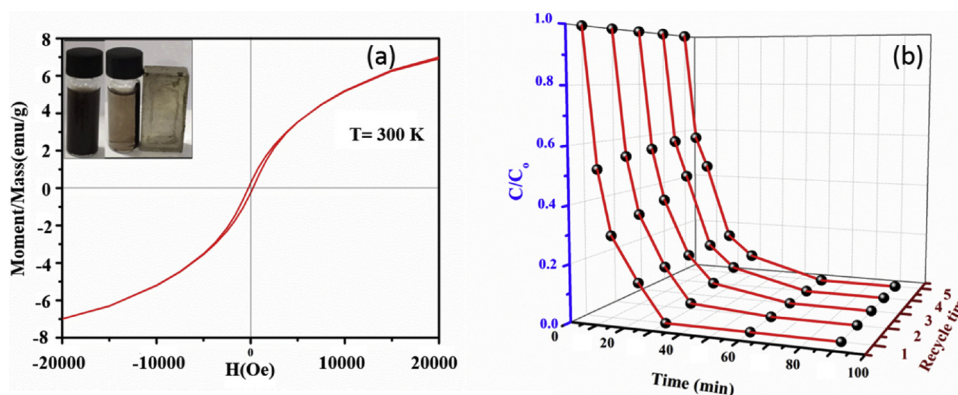Based on the above results, a probable mechanism of PMS activation

**Fig. 8.** (a) M−H hysteresis loop for γ-MnO$_2$@ZnFe$_2$O$_4$/rGO nanohybrid at 300 K and (b) reusability test of the γ-MnO$_2$@ZnFe$_2$O$_4$/rGO nanohybrid for the degradation of 20 ppm phenol using 0.2 g L$^{-1}$ catalyst and 2 g L$^{-1}$ PMS at 300 K for five successive cycles.
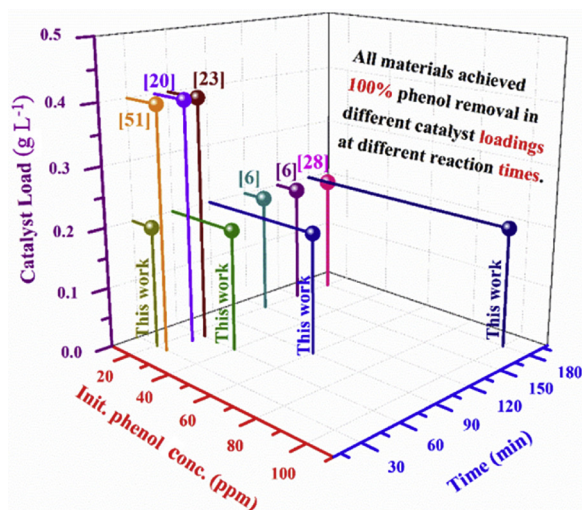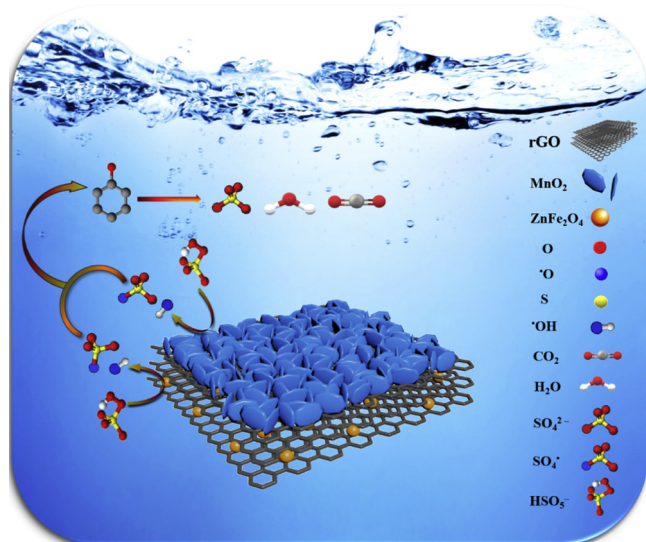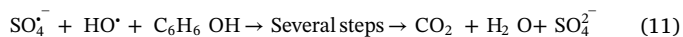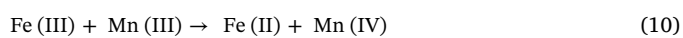


**Fig. 9.** Comparison of the performance of the catalysts containing MnO$_2$, ZnFe$_2$O$_4$ NPs, and RGO nanosheets reported in the literature and the present work.



**Scheme 2.** Schematic diagram of the proposed phenol degradation mechanism on the γ-MnO$_2$@ZnFe$_2$O$_4$/rGO nanohybr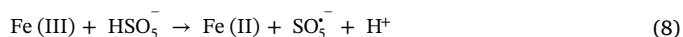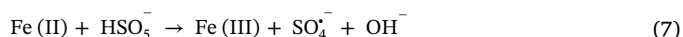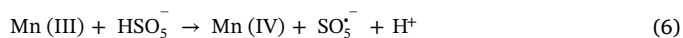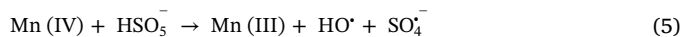id. Reaction conditions: catalyst loading = 0.2 g L$^{-1}$, PMS loading = 2.0 g L$^{-1}$ (3 mM), and temperature = 25 °C.

on the active sites of the γ-MnO$_2$@ZnFe$_2$O$_4$/rGO nanohybrid for phenol degradation can be proposed as follows (Eqs. (5)–(11) and Scheme 2):

$$Mn\,(IV) + HSO_5^- \rightarrow Mn\,(III) + HO^\bullet + SO_4^- \qquad (5)$$

$$Mn\,(III) + HSO_5^- \rightarrow Mn\,(IV) + SO_5^{\bullet-} + H^+ \qquad (6)$$

$$Fe\,(II) + HSO_5^- \rightarrow Fe\,(III) + SO_4^{\bullet-} + OH^- \qquad (7)$$

$$Fe\,(III) + HSO_5^- \rightarrow Fe\,(II) + SO_5^{\bullet-} + H^+ \qquad (8)$$

$$2SO_5^{\bullet-} + 2OH^- \rightarrow 2SO_4^{2-} + 2HO^\bullet + O_2 \qquad (9)$$

$$Fe\,(III) + Mn\,(III) \rightarrow Fe\,(II) + Mn\,(IV) \qquad (10)$$

$$SO_4^{\bullet-} + HO^\bullet + C_6H_6\,OH \rightarrow Several\,steps \rightarrow CO_2 + H_2O + SO_4^{2-} \qquad (11)$$
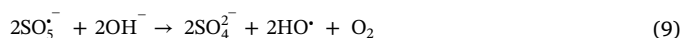
The Mn(IV)/Mn(III) and Fe(II)/Fe(III) transitions involve electron transfer, which is responsible for the catalytic reaction [20,23]. In the first stage, the active sites of both MnO$_2$ and ZnFe$_2$O$_4$ on the nanohybrid can activate PMS to generate active radicals (Eqs. (5)–(8)), which are responsible for phenol degradation (Eq. (11)) [25,52,53]. Hydroxyl radicals are generated (Eq. (9)) further after the depletion of SO$_4^-$ in a rapid reaction with phenol in the first stage, and HO$^\bullet$ becomes the only radical that reacts with phenol in the last stage of the reaction [22]. The return to the original oxidation states of the metals (Mn(IV) and Fe(II)) is due to the recovery reactions on the reduced hybrid (Eq. (10)).

## 4. Conclusions

A magnetically separable 3D γ-MnO$_2$@ZnFe$_2$O$_4$/rGO nanohybrid was synthesized using a facile hydrothermal method for phenol degradation in the presence of PMS as the source of active radicals. The γ-MnO$_2$@ZnFe$_2$O$_4$/rGO nanohybrid showed high catalytic efficiency compared to the other composites δ-MnO$_2$@ZnFe$_2$O$_4$, γ-MnO$_2$@rGO, and ZnFe$_2$O$_4$@rGO. This excellent catalytic activity was attributed to the synergetic effects of MnO$_2$, ZnFe$_2$O$_4$, and graphene and the high surface area of the catalyst for PMS activation. The degradation of phenol followed a first-order kinetic model with an activation energy of 41.5 kJ mol$^{-1}$. The PMS activation mechanism for the catalytic reaction was investigated by examining the contributions of the different active radicals (SO$_4^\bullet$ and HO$^\bullet$), and a probable mechanism of phenol degradation was proposed. The nanohybrid exhibited excellent reusability even after five degradation cycles due to the stability of the structure and its inherent magnetic property. Consequently, the γ-MnO$_2$@ZnFe$_2$O$_4$/rGO nanohybrid is expected to be an effective catalyst material in environmental treatment applications.

## Acknowledgments

## Appendix A. Supplementary data

Supplementary material related to this article can be found, in the online version, at doi:https://doi.org/10.1016/j.apcatb.2018.11.086.

## References

[1] L.F. Liotta, M. Gruttadauria, G. Di Carlo, G. Perrini, V. Librando, Heterogeneous catalytic degradation of phenolic substrates: catalysts activity, J. Hazard. Mater. 162 (2009) 588–606.

[2] E.M. Seftel, M. Niarchos, Ch. Mitropoulos, M. Mertens, E.F. Vansant, P. Cool, Photocatalytic removal of phenol and methylene-blue in aqueous media using TiO$_2$/LDH clay nanocomposites, Catal. Today 252 (2015) 120–127.

[3] C. Su, X. Duan, J. Miao, Y. Zhong, W. Zhou, S. Wang, Z. Shao, Mixed conducting perovskite materials as superior catalysts for fast aqueous-phase advanced oxidation: a mechanistic study, ACS Catal. 7 (2017) 388–397.

[4] F.Z. Yehia, Gh. Eshaq, A.M. Rabie, A.H. Mady, A.E. ElMetwally, Phenol degradation by advanced Fenton process in combination with ultrasonic irradiation, Egypt. J. Petrol. 24 (2015) 13–18.

[5] X. Duan, Z. Ao, H. Sun, S. Indrawirawan, Y. Wang, J. Kang, F. Liang, Z.H. Zhu, S. Wang, Nitrogen-doped graphene for generation and evolution of reactive radicals by metal-free catalysis, ACS Appl. Mater. Interfaces 7 (2015) 4169–4178.

[6] Y. Wang, H. Sun, H.M. Ang, M.O. Tadé, S. Wang, Facile synthesis of hierarchically structured magnetic MnO$_2$/ZnFe$_2$O$_4$ hybrid materials and their performance in heterogeneous activation of peroxymonosulfate, ACS Appl. Mater. Interfaces 6 (2014) 19914–19923.

[7] Y. Wang, Y. Xie, H. Sun, J. Xiao, H. Cao, S. Wang, 2D/2D nano-hybrids of γ- MnO$_2$ on reduced graphene oxide for catalytic ozonation and coupling peroxymonosulfate activation, J. Hazard. Mater. 301 (2016) 56–64.

[8] N. Novak Tušar, D. Maučec, M. Rangus, I. Arčon, M. Mazaj, M. Cotman, A. Pintar, V. Kaučič, Manganese functionalized silicate nanoparticles as a fenton-type catalyst for water purification by advanced oxidation processes (AOP), Adv. Funct. Mater. 22 (2012) 820–826.

[9] X. Duan, H. Sun, Y. Wang, J. Kang, S. Wang, N-doping-induced nonradical reaction on single-walled carbon nanotubes for catalytic phenol oxidation, ACS Catal. 5 (2015) 553–559.

[10] S.O. Ganiyu, M. Zhou, C.A. Martínez-Huitle, Heterogeneous electro-Fenton and photoelectro-Fenton processes: A critical review of fundamental principles and application for water/wastewater treatment, Appl. Catal. B: Environ. 235 (2018) 103–129.

[11] L. Clarizia, D. Russo, I. Di Somma, R. Marotta, R. Andreozzi, Homogeneous photo-Fenton processes at near neutral pH: a review, Appl. Catal. B: Environ. 209 (2017) 358–371.

[12] S. Yuan, Y. Fan, Y. Zhang, M. Tong, P. Liao, Pd-catalytic in situ generation of H$_2$O$_2$ from H$_2$ and O$_2$ produced by Water electrolysis for the efficient electro-fenton degradation of rhodamine B, Environ. Sci. Technol 45 (2011) 8514–8520.

[13] L. Tang, Y. Liu, J. Wang, G. Zeng, Y. Deng, H. Dong, H. Feng, J. Wang, B. Peng, Enhanced activation process of persulfate by mesoporous carbon for degradation of aqueous organic pollutants: electron transfer mechanism, Appl. Catal. B: Environ. 231 (2018) 1–10.

[14] L. Hu, X. Yang, S. Dang, An easily recyclable Co/SBA-15 catalyst: heterogeneous activation of peroxymonosulfate for the degradation of phenol in water, Appl. Catal. B: Environ. 102 (2011) 19–26.

[15] K.-Y.A. Lin, F.-K. Hsu, W.-D. Lee, Magnetic cobalt–graphene nanocomposite derived from self-assembly of MOFs with graphene oxide as an activator for peroxymonosulfate, J. Mater. Chem. A 3 (2015) 9480–9490.

[16] T. Zeng, X. Zhang, S. Wang, H. Niu, Y. Cai, Spatial confinement of a Co$_3$O$_4$ catalyst in hollow metal–organic frameworks as a nanoreactor for improved degradation of organic pollutants, Environ. Sci. Technol. 49 (2015) 2350–2357.

[17] W.-D. Oh, Z. Dong, Z.-T. Hu, T.-T. Lim, A novel quasi-cubic CuFe$_2$O$_4$–Fe$_2$O$_3$ catalyst prepared at low temperature for enhanced oxidation of bisphenol A *via* peroxymonosulfate activation, J. Mater. Chem. A 3 (2015) 22208–22217.

[18] S. Zhang, Q. Fan, H. Gao, Y. Huang, X. Liu, J. Li, X. Xu, X. Wang, Formation of Fe$_3$O$_4$/MnO$_2$ ball-in-ball hollow spheres as a high performance catalyst with enhanced catalytic performances, J. Mater. Chem. A 4 (2016) 1414–1422.

[19] W. Xiao, D. Wang, X.W. Lou, Shape-controlled synthesis of MnO$_2$ nanostructures with enhanced electrocatalytic activity for oxygen reduction, J. Phys. Chem. C 114 (2010) 1694–1700.

[20] E. Saputra, S. Muhammad, H. Sun, H.-M. Ang, M.O. Tadé, S. Wang, Shape-controlled activation of peroxymonosulfate by single crystal α-Mn$_2$O$_3$ for catalytic phenol degradation in aqueous solution, Appl. Catal. B: Environ. 154–155 (2014) 246–251.

[21] P. Yu, X. Zhang, D. Wang, L. Wang, Y. Ma, Shape-controlled synthesis of 3D hierarchical MnO$_2$ nanostructures for electrochemical supercapacitors, Cryst. Growth Des. 9 (2009) 528–533.

[22] Y. Wang, S. Indrawirawan, X. Duan, H. Sun, H.M. Ang, M.O. Tadé, S. Wang, New insights into heterogeneous generation and evolution processes of sulfate radicals for phenol degradation over one-dimensional α-MnO$_2$ nanostructures, Chem. Eng. J. 266 (2015) 12–20.

[23] E. Saputra, S. Muhammad, H. Sun, H.-M. Ang, M.O. Tadé, S. Wang, Manganese oxides at different oxidation states for heterogeneous activation of peroxymonosulfate for phenol degradation in aqueous solutions, Appl. Catal. B: Environ. 142–143 (2013) 729–735.

[24] P. Guo, L. Cui, Y. Wang, M. Lv, B. Wang, X.S. Zhao, Facile synthesis of ZnFe$_2$O$_4$ nanoparticles with tunable magnetic and sensing properties, Langmuir 29 (2013) 8997–9003.

[25] M. Feng, R. Qu, X. Zhang, P. Sun, Y. Sui, L. Wang, Z. Wang, Degradation of flumequine in aqueous solution by persulfate activated with common methods and polyhydroquinone-coated magnetite/multi-walled carbon nanotubes catalysts, Water Res. 85 (2015) 1–10.

[26] H. Xu, J. Jia, Y. Guo, Z. Qu, Y. Liao, J. Xie, W. Shangguan, N. Yan, Design of 3D MnO$_2$/Carbon sphere composite for the catalytic oxidation and adsorption of elemental mercury, J. Hazard. Mater. 342 (2018) 69–76.

[27] Y. Wang, H. Sun, H.M. Ang, M.O. Tadé, S. Wang, 3D-hierarchically structured MnO$_2$ for catalytic oxidation of phenol solutions by activation of peroxymonosulfate: structure dependence and mechanism, Appl. Catal. B: Environ. 164 (2015) 159–167.

[28] Y. Wang, Y. Xie, C. Chen, X. Duan, H. Sun, S. Wang, Synthesis of magnetic carbon supported manganese catalysts for phenol oxidation by activation of peroxymonosulfate, Catalysts 7 (2017) 3.

[29] A.H. Mady, M.L. Baynosa, D. Tuma, J.-J. Shim, Facile microwave-assisted green synthesis of Ag-ZnFe$_2$O$_4$/rGO nanocomposites for efficient removal of organic dyes under UV- and visible-light irradiation, Appl. Catal. B: Environ. 203 (2017) 416–427.

[30] J. Qu, L. Shi, C. He, F. Gao, B. Li, Q. Zhou, H. Hu, G. Shao, X. Wang, J. Qiu, Highly efficient synthesis of graphene/MnO$_2$ hybrids and their application for ultrafast oxidative decomposition of methylene blue, Carbon 66 (2014) 485–492.

[31] M.M. Kadam, K.B. Dhopte, N. Jha, V.G. Gaikar, P.R. Nemade, Synthesis, characterization and application of γ-MnO$_2$/graphene oxide for the selective aerobic oxidation of benzyl alcohols to corresponding carbonyl compounds, New J. Chem. 40 (2016) 1436–1442.

[32] M. Ramesh, M. Purnachander Rao, F. Rossignol, H.S. Nagaraja, rGO/MnO$_2$ nanowires for ultrasonic-combined fenton assisted efficient degradation of reactive Black 5, Water Sci. Technol. 76 (2017) 1652–1665.

[33] D.C. Marcano, D.V. Kosynkin, J.M. Berlin, A. Sinitskii, Z. Sun, A. Slesarev, L.B. Alemany, W. Lu, J.M. Tour, Improved synthesis of graphene oxide, ACS Nano 4 (2010) 4806–4814 12 (2018) 2078.

[34] G.-Y. Zhang, Y.-Q. Sun, D.-Z. Gao, Y.-Y. Xu, Quasi-cube ZnFe$_2$O$_4$ nanocrystals: hydrothermal synthesis and photocatalytic activity with TiO$_2$ (Degussa P25) as nanocomposite, Mater. Res. Bull. 45 (2010) 755–760.

[35] J. Shao, W. Li, X. Zhou, J. Hu, Magnetic-field-assisted hydrothermal synthesis of 2 × 2 tunnels of MnO$_2$ nanostructures with enhanced supercapacitor performance, Cryst. Eng. Comm. 16 (2014) 9987–9991.

[36] C. Julien, M. Massot, S. Rangan, M. Lemal, D. Guyomard, Study of structural defects in γ-MnO$_2$ by Raman spectroscopy, J. Raman Spectrosc. 33 (2002) 223–228.

[37] L. Li, Z. Guo, A. Du, H. Liu, Rapid microwave-assisted synthesis of Mn$_3$O$_4$–graphene nanocomposite and its lithium storage properties, J. Mater. Chem. 22 (2012) 3600–3605.

[38] Y. Zhao, W. Ran, J. He, Y. Huang, Z. Liu, W. Liu, Y. Tang, L. Zhang, D. Gao, F. Gao, High-performance asymmetric supercapacitors based on multilayer MnO$_2$/graphene oxide nanoflakes and hierarchical porous carbon with enhanced cycling stability, Small 11 (2015) 1310–1319.

[39] W.T. Huang, H. Zhang, Y. Huang, W. Wang, S. Wei, Hierarchical porous carbon obtained from animal bone and evaluation in electric double-layer capacitors, Carbon 49 (2010) 838–843.

[40] Z. Fan, J. Yan, T. Wei, L. Zhi, G. Ning, T. Li, F. Wei, Asymmetric supercapacitors based on graphene/MnO$_2$ and activated carbon nanofiber electrodes with High power and energy density, Adv. Funct. Mater. 21 (2011) 2366–2375.

[41] Y. Li, X. Qin, T. Wang, L. Ma, L. Chen, N. Tsubaki, Fischer-Tropsch synthesis from H$_2$-deficient biosyngas over Mn added Co/SiO$_2$ catalysts, Fuel 136 (2014) 130–135.

[42] Z. Lei, F. Shi, L. Lu, Incorporation of MnO$_2$-coated carbon nanotubes between graphene sheets as supercapacitor electrode, ACS Appl. Mater. Interfaces 4 (2012) 1058–1064.

[43] Y. Wang, H. Sun, H.M. Ang, M.O. Tadé, S. Wang, Magnetic Fe$_3$O$_4$/carbon sphere/cobalt composites for catalytic oxidation of phenol solutions with sulfate radicals, Chem. Eng. J. 245 (2014) 1–9.

[44] E. Saputra, H. Zhang, Q. Liu, H. Sun, S. Wang, Egg-shaped core/shell α-Mn$_2$O$_3$/α-MnO$_2$ as heterogeneous catalysts for decomposition of phenolics in aqueous solutions, Chemosphere 159 (2016) 351–358.

[45] S.D. Perera, R.G. Mariano, K. Vu, N. Nour, O. Seitz, Y. Chabal, K.J. Balkus Jr., Hydrothermal synthesis of graphene-TiO2 nanotube composites with enhanced photocatalytic activity, ACS Catal. 2 (2012) 949–956.

[46] X. Duan, K. O'Donnell, H. Sun, Y. Wang, S. Wang, Sulfur and nitrogen Co-doped graphene for metal-free catalytic oxidation reactions, Small 11 (2015) 3036–3044.

[47] W.D. Oh, Z. Dong, T.-T. Lim, Generation of sulfate radical through heterogeneous catalysis for organic contaminants removal: current development, challenges and prospects, Appl. Catal. B: Environ. 194 (2016) 169–201.

[48] E. Hayon, A. Treinin, J. Wilf, Electronic spectra, photochemistry, and autoxidation

mechanism of the sulfite-bisulfite-pyrosulfite systems. The $SO_2^-$, $SO_3^-$, $SO_4^-$, and $SO_5^-$ radicals, J. Amer. Chem. Soc. 94 (1972) 47–57.

[49] R.O.C. Norman, P.M. Storey, P.R. West, Electron spin resonance studies. Part XXV. Reactions of the sulphate radical anion with organic compounds, J. Chem. Soc. (B) (1970) 1087–1095.

[50] L. Dogliotti, E. Hayon, Flash photolysis of persulfate ions in aqueous solutions. Study of the sulfate and ozonide radical anions, J. Phys. Chem. 71 (1967) 2511–2516.

[51] E. Saputra, S. Muhammad, H. Sun, H.-M. Ang, M.O. Tadé, S.B. Wang, A comparative study of spinel structured $Mn_3O_4$, $Co_3O_4$ and $Fe_3O_4$ nanoparticles in catalytic

oxidation of phenolic contaminants in aqueous solutions, J. Colloid Interface Sci. 407 (2013) 467–473.

[52] D. Chen, X. Ma, J. Zhou, X. Chen, G. Qian, Sulfate radical-induced degradation of acid orange 7 by a new magnetic composite catalyzed peroxymonosulfate oxidation process, J. Hazard. Mater. 279 (2014) 476–484.

[53] C.M. Park, J. Heo, D. Wang, C. Su, Y. Yoon, Heterogeneous activation of persulfate by reduced graphene oxide–elemental silver/magnetite nanohybrids for the oxidative degradation of pharmaceuticals and endocrine disrupting compounds in water, Appl. Catal. B: Environ. 225 (2018) 91–99.